Nanoscale

Lead-Free Double Perovskites $Cs_2InCuCl_6$ and $(CH_3NH_3)_2InCuCl_6$: Electronic, Optical, and Electrical Properties

Journal:	*Nanoscale*
Manuscript ID	NR-ART-02-2019-001645.R2
Article Type:	Paper
Date Submitted by the Author:	07-May-2019

Complete List of Authors:	Pham, Hung; University of Minnesota System, Chemistry Holmes, Russell; University of Minnesota, Chemical Engineering and Materials Science Aydil, Eray; New York University Tandon School of Engineering, Department of Chemical and Biomolecular Engineering Gagliardi, Laura; University of Minnesota, Department of Chemistry and Supercomputing Institute

ARTICLE

Lead-Free Double Perovskites $Cs_2InCuCl_6$ and $(CH_3NH_3)_2InCuCl_6$: Electronic, Optical, and Electrical Properties

Received 00th January 20xx,
Accepted 00th January 20xx

DOI: 10.1039/x0xx00000x

Hung Q. Pham,[a] Russell J. Holmes,[b] Eray S. Aydil[c] and Laura Gagliardi*[a]

Searching for alternatives to lead-containing metal halide perovskites, we explored the properties of indium-based inorganic double perovskites Cs_2InMX_6 with M = Cu, Ag, Au and X = Cl, Br, I, and of its organic-inorganic hybrid derivative $MA_2InCuCl_6$ ($MA = CH_3NH_3^+$) using computation within Kohn-Sham density functional theory. Among these compounds, $Cs_2InCuCl_6$ and $MA_2InCuCl_6$ were found as potentially promising candidates for solar cells. Calculations with different functionals bound the direct band gap of $Cs_2InCuCl_6$ between 1.05 and 1.73 eV. In contrast, $MA_2InCuCl_6$ exhibits an indirect band gap between 1.31 and 2.09 eV depending on the choice of exchange-correlation functional. $Cs_2InCuCl_6$ exhibits a much higher absorption coefficient than that calculated for c-Si and CdTe, common semiconductors for solar cells. Even $MA_2InCuCl_6$ is predicted to have a higher absorption coefficient than c-Si and CdTe across the visible spectrum despite the fact that it is an indirect band gap material. The intrinsic charge carrier mobilities for $Cs_2InCuCl_6$ along the L-Γ path are predicted to be comparable to those for $MAPbI_3$. Finally, we carried out calculations of the band edge positions for $MA_2InCuCl_6$ and $Cs_2InCuCl_6$ to offer guidance for solar cell heterojunction design and optimization. We conclude that $Cs_2InCuCl_6$ and $MA_2InCuCl_6$ are promising semiconductors for photovoltaic and optoelectronic applications.

1. Introduction

Metal halide perovskites with the chemical formula ABX_3 where A is an inorganic or organic cation (*e.g.,* Cs^+, $CH_3NH_3^+$, *etc.*), B a metal (*e.g.,* Pb, Sn, *etc.*), and X a halogen (*e.g.,* Cl, Br, or I), are being vigorously explored as materials for low-cost and high efficiency solar cells.[1-3] The flurry of activity over this class or materials is fuelled by the remarkable increase in power conversion efficiency (PCE) for solar cells based on methylammonium lead iodide ($CH_3NH_3PbI_3$ or $MAPbI_3$) from 3.8% in 2009,[4] to a record 23.3% in less than a decade.[5-9] These efficiencies are already exceeding the performance of conventional thin film photovoltaic devices based on cadmium telluride (CdTe) and copper indium gallium diselenide (CIGS).[6] Importantly, tandem solar cells based on metal halide perovskites are rivalling even crystalline silicon (c-Si) in performance, with PCEs >26% achieved in preliminary devices.[10-12] This astounding high efficiency together with their solution processability[13] places metal-halide perovskite-based photovoltaics at the forefront of progress in solar photoconversion. It is also becoming clear that metal halide perovskites have broader appeal in applications beyond photovoltaics, and recent research has demonstrated a variety of electronic and optoelectronic devices including transistors,[14, 15] light emitting diodes,[16-18] and lasers.[19, 20] Lead containing perovskites, however, face two problems, their limited chemical stability[21, 22] and the negative impact, real or perceived, of lead on the environment and human health.[23, 24] Rong *et al.*[25] discussed these challenges in a recent review. These issues have motivated a search for lead-free, non-toxic alternatives to $MAPbI_3$. Strategies, pursued both experimentally and *via* computational screening, include but are not limited to substituting lead in $APbX_3$ with non-toxic metals,[26-29] exploring structures derived from the aristotype cubic perovskite (*e.g.,* layered perovskites, double perovskite, vacancy-ordered double perovskites, *etc.*),[30, 31] and designing new perovskite-inspired materials such as inverse[32] or metal-free perovskites.[33] Amongst these materials, double perovskites with the general formula $A_2B_1B_2X_6$ where B_1 and B_2 are formally (3+) and (1+) metallic cations, respectively, have drawn our attention because their chemical diversity can be exploited to tune optoelectronic functionality. Recently, the inorganic double perovskite $Cs_2InAgCl_6$ has been synthesized and claimed to have a direct band gap but its value, 3.3 eV, is too large for application in solar cells.[34, 35] The analogous $Cs_2InAgBr_6$ should have a narrower band gap and has been claimed to be stable *via* DFT calculations[36] but it has not yet been synthesized. When Bi or Sb is substituted for In, the band gap narrows to ~ 2 eV but also becomes indirect.[37-41] A band gap of 2 eV is still too high for solar cell applications though these materials could be used as the wide gap layer in tandem solar cells. Despite their potential for light harvesting applications, other indium-based

[a] Department of Chemistry, Chemical Theory Center, and Supercomputing Institute, University of Minnesota, 207 Pleasant Street SE, Minneapolis, Minnesota 55455, United States.
[b] Department of Chemical Engineering and Materials Science, University of Minnesota, 421 Washington Ave. SE, Minneapolis, Minnesota 55455, United States.
[c] Department of Chemical and Biomolecular Engineering, New York University, Tandon School of Engineering, 6 Metrotech Center, Brooklyn, New York 11201, United States.

† Electronic Supplementary Information (ESI) available: optimized crystal structures, computational details for c-Si and CdTe, Goldschmidt's criteria calculation, detailed computation for band edge positions, optical absorption coefficient, and charge carrier mobility. See DOI: 10.1039/x0xx00000x

double perovskites have not been investigated in detail. Accordingly, we focus on A_2InMX_6 (A = Cs^+, MA^+, M = Cu, Ag, Au and X = Cl, Br) and examine their potential for solar cells. The more general question 'what makes a good solar cell?' has been addressed elsewhere.[42] Briefly, materials suitable for solar cells must exhibit high optical absorption, a band gap located within the broad maximum of the Shockley-Queisser-limit curve (1.0-1.6 eV),[43, 44] good charge transport properties, and high chemical stability.[42] Indeed, lead halide perovskites are excellent light absorbers with tunable band gaps, long charge carrier lifetimes and diffusion lengths, and high defect tolerance.[1] These are the characteristics that must be examined when seeking an alternative to lead halide perovskites.

We first screened a series of indium-based inorganic double perovskites Cs_2InMX_6 with M = Cu, Ag, Au and X = Cl, Br, I by means of Kohn-Sham density functional theory[45-47] and searched for materials with band gaps in the 1.0 - 2.0 eV range. We chose the combination of In(III) and M(I) metal instead of In(I) and M(III) because In(I)-based double perovskites are unstable owing to the oxidation of In(I) to In(III).[48] This prescreening identified $Cs_2InCuCl_6$ as a potential candidate with a band gap in the 1.05 - 1.73 eV range (depending on the method used for calculation). To inspect the influence of organic cations, we also studied the organic-inorganic hybrid, $MA_2InCuCl_6$ by replacing Cs^+ with the methylammonium ($MA = CH_3NH_3^+$) cation and considering different orientations of MA in the octahedral cages. While some articles on Cu-In double perovskites have been published,[49, 50] $Cs_2InCuCl_6$ and $MA_2InCuCl_6$, have not been studied systematically and in detail as is done here. In particular, we evaluated the electronic structure, optical absorption coefficient, and intrinsic charge carrier mobility of $Cs_2InCuCl_6$ and $MA_2InCuCl_6$.

2. Computational methods

2.1 Kohn-Sham DFT calculations

Kohn-Sham density functional theory (KS-DFT)[45-47] calculations were performed using the Vienna Ab initio Simulation Package (VASP).[51-54] To optimize the crystal structures, the PBEsol[55] exchange-correlation functional was employed and a kinetic energy cutoff of 500 eV was used. The convergence criteria for total energy and Hellmann−Feynman force were set to 10^{-6} eV and 10^{-3} eV/Å, respectively. For $Cs_2InCuBr_6$ and $Cs_2InAuBr_6$, a weaker force of 10^{-2} eV/Å was used due to a difficulty in locating the minimum energy points of these structures. A Gamma centered grid of 10 × 10 × 10 was used to sample the first Brillouin zone (FBZ). For the band gap screening, the standard HSE06[56] functional (*i.e.* the screening parameter of 0.2 $Å^{-1}$ and the exact exchange of 25%) including spin-orbit coupling (SOC), was used with a 4 × 4 × 4 k-mesh. A kinetic cutoff of 400 eV and an energy threshold of 10^{-5} eV were employed. After screening, for $Cs_2InCuCl_6$ and $MA_2InCuCl_6$ the HSE06-SOC and PBE0-SOC[57] were employed to compute their band gaps using a stricter energy threshold of 10^{-6} eV. We computed the phonon band structure for $Cs_2InCuCl_6$ by using Phonopy.[58] The phonon calculation was performed using a 2 × 2 × 2 supercell and a 5 × 5 × 5 k-mesh and with the forces computed at the PBEsol level by VASP using a strict energy criteria of 10^{-10} eV. Small negative acoustic phonons modes at the Γ point, caused by the imperfection of translational symmetry used in the force calculation, were corrected by symmetrizing the calculated forces using the keyword FC_SYMMETRY = 1 in the Phonopy configuration file. Optical absorption coefficients were computed using the PBE[59, 60] functional and a dense 30 × 30 × 30 k-mesh. We applied a simple scissor correction in plotting the absorption coefficient using the HSE06-SOC and PBE0-SOC band gaps instead of the band gap by PBE functional which suffers from the self-interaction error.[61-63] In order to relax the $MA_2InCuCl_6$ structures, we first optimized the unit cell size and ion positions while keeping the cell shape unchanged using CRYSTAL17[64] and the triple-zeta basis set with polarization quality pob-TZVP[65, 66] for all the elements. We used CRYSTAL here to preserve the crystal system, *i.e.* cubic, of the structure during the geometrical relaxation because VASP does not support this function. Next, using VASP, we relaxed the ion positions and the lattice parameters while keeping the cell shape unchanged. Within this approach, the optimized $MA_2InCuCl_6$ (HA or HB) structure has the same computational cubic unit cell as $Cs_2InCuCl_6$ and their corresponding FBZ can be sampled with the same paths when analyzing the band structure. Computational details for standard semiconductors such as c-Si and CdTe are provided in Section S1 of the Supplementary Information (**SI**).

2.1 Charge transport calculations

The intrinsic charge carrier mobility was calculated using the Boltzmann Transport Equation (BTE)[67] in conjunction with the Deformation Potential (DP)[68] theory. In this approach, the acoustic phonon scattering is the only mechanism considered in computing the relaxation time and the mobility μ is given by

$$\mu = \frac{2(2\pi)^{1/2} e\hbar^4 C}{3E_1^2 (k_B T)^{3/2} (m^*)^{5/2}}$$

where C, E_1, m^*, e, $\hbar$, k_B, and T are the elastic constant, the DP constant, the effective mass, the elementary charge, the reduced Planck constant, the Boltzmann constant, and temperature, respectively. To compute the DP constant, E_1, the band edge energy shift with respect to the dilation, $\Delta l/l_o$ (where l_o, Δl are the equilibrium lattice parameter and its change caused by the strain, respectively), was fitted using linear regression. The elastic constant C was obtained by fitting a parabola to the variation of the unit cell electronic energy E with respect to the dilation $\Delta l/l_o$ around the equilibrium point, l_o. The effective masses of the holes and the electrons were calculated from the curvatures of the parabolas fitted to the variation of the valence (for holes) and conduction band (for electrons) edge energies with respect to the momentum k (*i.e.,* E(k) dispersion). See Section S5 of the **SI** for details.

3. Results and discussions

3.1 Band gap screening

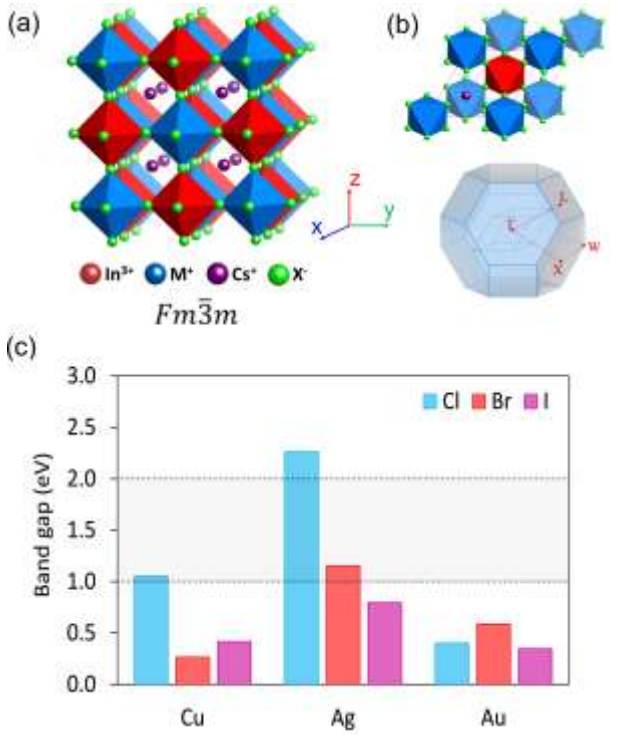

Fig. 1 (a) Double perovskite Cs_2InMX_6 structure (M = Cu, Ag, Au and X = Cl, Br, I) with MX_6 and InX_6 octahedra depicted as blue and red, respectively. (b) Cs_2InMX_6 primitive unit cell and the corresponding first Brillouin zone (FBZ). (c) Calculated band gaps for Cs_2InMX_6.

First, we screened different M and X in the Cs_2InMX_6 structure (M = Cu, Ag, Au and X = Cl, Br, I) to identify those compounds with band gap in the 1.0-2.0 eV range. All structures were taken to be cubic as all experimentally reported double-perovskites have a cubic structure. Fig. 1a shows the Cs_2InMX_6 primitive unit cell used in the calculation, and the corresponding first Brillouin zone (FBZ). We calculated the Goldschmidt's empirical factors[69] to evaluate the relative stability of these hypothetical compounds before performing extensive electronic structure calculations (see the **SI** Section S2 Fig. S1). The tolerance and octahedral factors predict that most of these perovskite structures should be stable except for Cs_2InCuI_6: the octahedral factor for Cs_2InCuI_6 is slightly smaller than the requisite value, 0.41. According to the Shockley-Queisser limit,[43, 44] a solar cell based on a semiconductor with a band gap of 1.0-1.6 eV will have a maximum efficiency of 30-33%. We choose a wider range, 1.0-2.0 eV, for screening because the exchange-correlation functional approximation carries uncertainties in predicting band gap, and many photovoltaic semiconductors have band gaps falling within this range including crystalline silicon c-Si (1.17 eV),[70] CdTe (1.61 eV),[71] CdSe (1.74 eV),[70] GaAs (1.52 eV),[70] *etc.* Of the nine compounds considered, only $Cs_2InCuCl_6$ and $Cs_2InAgBr_6$ have band gaps falling in this range. Previous computational studies predicted the band gap of $Cs_2InAgBr_6$ to be 1.0-2.0 eV[34, 36] and already identified this compound as a potential solar absorber, thus we do not consider this compound any further in our study. Fig. 2 shows the phonon band structure for $Cs_2InCuCl_6$.

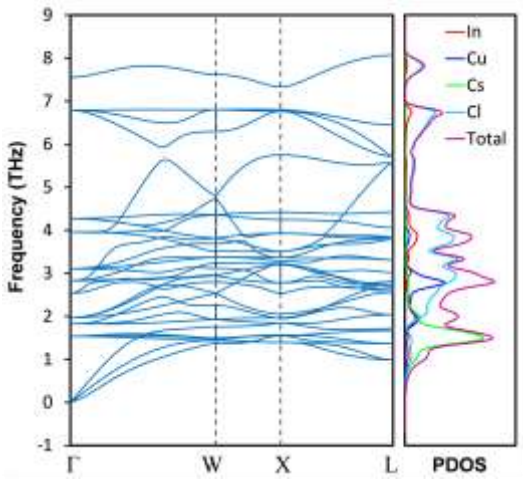

Fig. 2 Phonon band structure in the FBZ (left) and partial density of states (right) of $Cs_2InCuCl_6$.

These calculations predict several vibrational modes in the 50-150 cm^{-1} range and at ~225 cm^{-1} that could be detected using low-frequency Raman spectroscopy. There are no imaginary modes in the entire FBZ, establishing the dynamical stability of $Cs_2InCuCl_6$ in its cubic phase. This is different from $CsPbI_3$ where there are imaginary phonon modes in its phonon dispersion curve triggering the phase transition as temperature or pressure changes.[72] In addition, we compute the decomposition enthalpy (ΔH_d) considering several possible pathways by means of the PBEsol functional (Table 1). Our results show that most of the decomposition reactions are thermodynamically unfavorable except for reaction (5) which has negative ΔH_d. Also, the entropy and kinetic factors are not considered and the negative ΔH_d is quite small (ca. -3.7 kcal/mol/formula unit). Hence, we conclude that $Cs_2InCuCl_6$ is thermodynamically metastable. It is worth nothing that a previous combined DFT and experiment study by Xiao *et al.*[73] has concluded that Cu(I) double perovskites Cs_2InCuX_6 are thermodynamically unstable owing to the high energy of 3d state of Cu. However, their DFT calculations were performed using PBE approximation which has been proved to be inaccurate for double perovskites' thermodynamic stability prediction.[74] While we agree on the trend that other structures in the series with large anions might be unstable, we anticipate that $Cs_2InCuCl_6$ may be stable and further attempts on synthesizing it may be warranted, particularly in the thin film form where metastable states maybe stabilized kinetically or thermodynamically on appropriate substrates. Having found $Cs_2InCuCl_6$ to be stable and to have a suitable band gap, we investigated its other properties as well as the properties of its organic-inorganic hybrid derivative $MA_2InCuCl_6$, which are discussed next.

Table 1 Calculated decomposition enthalpies for $Cs_2InCuCl_6$.

Decomposition pathway	ΔH_d (meV)/atom
(1) $Cs_2InCuCl_6 \rightarrow InCl_3 + 2\ CsCl + CuCl$	67.4
(2) $Cs_2InCuCl_6 \rightarrow ½\ CsCu_2Cl_3 + ½\ Cs_3In_2Cl_9$	16.2
(3) $Cs_2InCuCl_6 \rightarrow ½\ CsCl + CuCl + ½\ Cs_3In_2Cl_9$	0.4
(4) $Cs_2InCuCl_6 \rightarrow ½\ Cs_3Cu_2Cl_5 + ½\ CsCl + InCl_3$	38.1
(5) $Cs_2InCuCl_6 \rightarrow ½\ Cs_3Cu_2Cl_5 + ⅛\ Cs_3In_2Cl_9 + ⅔\ InCl_3$	-16.2

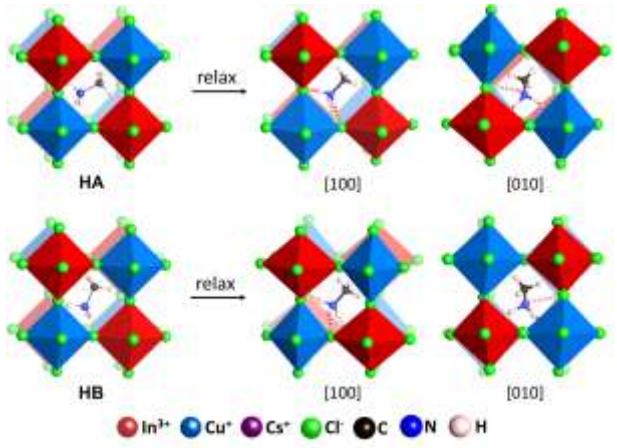

Fig. 3 Initial and final optimized structures of two possible configurations of $(MA)_2InCuCl_6$ along [100] and [010] direction. The red dash line depicts hydrogen bonding.

3.2 Geometrical and electronic structures

One of the main challenges in simulating hybrid halide perovskites is the dynamic disorder caused by the $CH_3NH_3^+$ cation.[75-78] Due to small energy barriers between its multiple isoenergetic local minima at different orientations, the $CH_3NH_3^+$ cations can rotate almost freely within the cuboctahedral cavity of the inorganic framework. There are two possible approaches to account for structural dynamic disorder. In one approach, one can perform dynamics simulations (either *ab initio* or classical) to directly capture the structural dynamics of the system, followed by the electronic structure calculations for some selected configurations.[79] This approach allows one to calculate the time-averaged properties of the system, which produces results such as the density of states broadening in $MAPbI_3$[80] or the phase transitions from the cubic to tetragonal and from tetragonal to orthorhombic phases upon cooling[81] all challenging to capture using static calculations. The electronic structure, however, becomes difficult to analyze because of symmetry breaking in dynamic simulations. Alternatively, in a second approach, one can consider several dominant dynamic orientations of the $CH_3NH_3^+$ ions from X-ray diffraction and identify a few important local minima using static DFT calculations, while preserving the crystallographic symmetry.[82-85] Recently, by sampling different configurations in the energy landscape Tan *et al.*[86] have found that there exist a few dominant configurations of $MAPbI_3$ at room temperature due to the hydrogen bonding and lattice distortion. Following this idea, we constructed $MA_2InCuCl_6$ from the $Cs_2InCuCl_6$ primitive cell by considering two most dominant orientations of $CH_3NH_3^+$ inside the octahedral cage, namely HA and HB as shown in Fig. 3. Although the initial structures for $MA_2InCuCl_6$ have no distortion of the MCl_6 octahedra in comparison to the $Cs_2InCuCl_6$ structure, the final optimized structures show slightly distorted MCl_6 units and a rearrangement of the $CH_3NH_3^+$ ions (Fig. 3). This distortion is presumably because of the hydrogen bonding between the N-H groups of the $CH_3NH_3^+$ ions and the Cl atoms of the MCl_6 units, which has been observed in $MAPbI_3$.[87] Additionally, we find that $MA_2InCuCl_6$ (HB) is 0.05 eV lower in energy than $MA_2InCuCl_6$ (HA), hence they are isoenergetic within the limits of the density functional approximation.

Table 2 Calculated band gaps (in eV) of $Cs_2InCuCl_6$ and $(MA)_2InCuCl_6$ in comparison with c-Si and CdTe.

	Calculated Band Gap (eV)	Band Gap	Experimental Band Gap (eV)
c-Si	1.19[c]	Indirect	1.17[d]
$Cs_2InCuCl_6$	1.05[a] – 1.73[b]	Direct	
$(MA)_2InCuCl_6$ (HA)	1.31[a] – 1.98[b]	Indirect	
$(MA)_2InCuCl_6$ (HB)	1.43[a] – 2.09[b]	Indirect	
CdTe	1.57[c]	Direct	1.61[d]

[a]HSE-SOC, [b]PBE0-SOC, [c]HSE06. [d]The experimental data are from ref 62 and 63.

A previous study showed that HSE06 and PBE0 can provide lower and upper bounds for the band gaps of halide double perovskites, respectively.[34] Hence, we calculated band gaps for $Cs_2InCuCl_6$ and $MA_2InCuCl_6$ (HA and HB) using both HSE06-SOC and PBE0-SOC (Table 2). Using this approach, we place the lower and upper limits on $Cs_2InCuCl_6$ band gap at 1.05 and 1.73

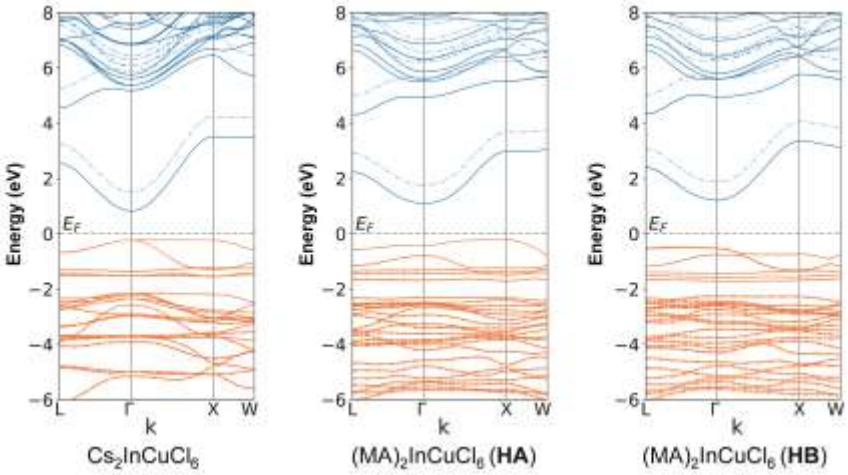

Fig. 4 Electronic band structure of $Cs_2InCuCl_6$ and $(MA)_2InCuCl_6$ (HA and HB) plotted along the high symmetry points, *i.e.*, L[1/2,1/2,1/2], Γ[0,0,0], X[1/2,0,1/2], W[1/2,1/4,3/4]. The valence bands and conduction bands are in orange and blue, respectively. The HSE06-SOC band structures are depicted by solid curves while the PBE0-SOC band structures are depicted by dash-dot curves. The Fermi energy is shifted to 0 eV.

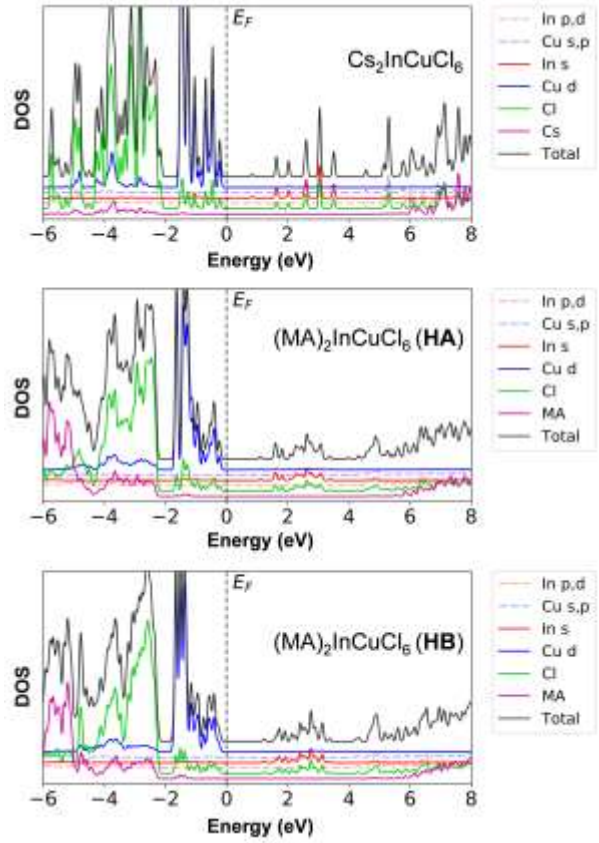

Fig. 5 HSE06-SOC density of states for $Cs_2InCuCl_6$ and $(MA)_2InCuCl_6$ (HA and HB). The Fermi energy is shifted to 0 eV.

eV, respectively, within the broad maximum of the Shockley-Queisser-limit curve. The limits on $MA_2InCuCl_6$ band gap are about 0.3 eV larger. There is no significant difference in the band gaps for the HA and HB configurations; the band gap calculated using the HB configuration is approximately 0.1 eV larger than that calculated using the HA configuration. Interestingly, we find that there is a direct-to-indirect transition of band gap in going from $Cs_2InCuCl_6$ to $MA_2InCuCl_6$. That is $Cs_2InCuCl_6$ is a direct band gap semiconductor while $MA_2InCuCl_6$ has an indirect band gap. The conduction band minimum (CBM) for all the structures are at the Γ point, while the valence band maximum (VBM) for $Cs_2InCuCl_6$, $MA_2InCuCl_6$ (HA), and $MA_2InCuCl_6$ (HB) are at the Γ, X, and L points, respectively (Fig. 4). The difference between the indirect and direct band gap for $MA_2InCuCl_6$ (HA and HB) are reported in the **SI** Section S4. In the following, we analyze and discuss the band structures to give insight into this direct-to-indirect transition. Fig. 4 shows the electronic band structures for $Cs_2InCuCl_6$ and $MA_2InCuCl_6$ (HA and HB). For $Cs_2InCuCl_6$, the valence band along the Γ-X path is flat. This is expected for indium-containing inorganic double perovskites due to the

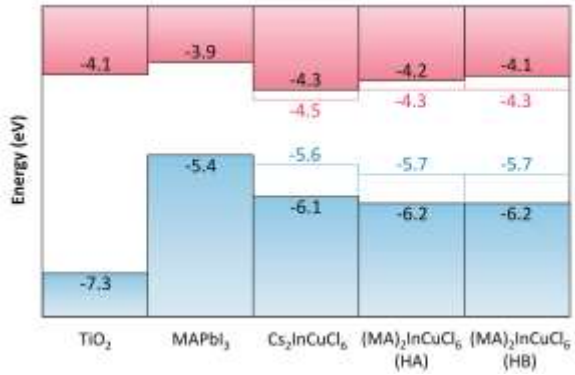

Fig. 6 Absolute band edge positions for $Cs_2InCuCl_6$ and $(MA)_2InCuCl_6$ using HSE06 (dash line) and PBE0 (solid line) functional. The values for TiO_2 and $MAPbI_3$ are taken from the ref 87 and shown for comparison.

two-dimensional character of the wave function.[34] For $MA_2InCuCl_6$, the $CH_3NH_3^+$ distorts the MCl_6 units as shown in Fig. 3, splitting the highest and the second highest valence bands along the L-Γ direction. Consequently, the two non-degenerate valence bands are observed in the entire FBZ of $MA_2InCuCl_6$ (HA and HB). Because of this distortion and the presence of $CH_3NH_3^+$ in the cuboctahedral cavities, $MA_2InCuCl_6$ structures have lower symmetry ($P1$) compared to the highly symmetric $Cs_2InCuCl_6$ ($Fm\bar{3}m$). This symmetry breaking, upon substitution of Cs^+ with $CH_3NH_3^+$, pushes the top of the valence band to the X and L points in $MA_2InCuCl_6$ (HA) and $MA_2InCuCl_6$ (HB), respectively, and ultimately causes the direct-to-indirect transition of the band gap. This interpretation is further informed by analyzing the density of states (see Fig. 5). We only present the HSE06-SOC density of states because the band *curvatures by HSE06-SOC and PBE0-SOC look alike as shown in* Fig. 4, implying that the PBE0-SOC density of states, if computed, will look identical to that by HSE06-SOC except for the difference in the band gap. In fact, $CH_3NH_3^+$ does not contribute to the band edges (*i.e.*, CBM and VBM) of $MA_2InCuCl_6$, similar to the insignificant role of Cs^+ in the CBM and VBM of $Cs_2InCuCl_6$. For both $Cs_2InCuCl_6$ and $MA_2InCuCl_6$, the CB is composed of the In *s* and Cl *p* orbitals while the VB is composed of the Cu *d* and Cl *p* orbitals (Fig. 5). In addition, we find that there is a density of states broadening in the conduction band of $MA_2InCuCl_6$ in comparison to that of $Cs_2InCuCl_6$. To confirm whether this is a consequence of the lower symmetry or an intrinsic property of $MA_2InCuCl_6$, we would need to perform a dynamic simulation or experimentally determine the density of states, which is beyond the scope of the current study.

3.3 Absolute band edge positions

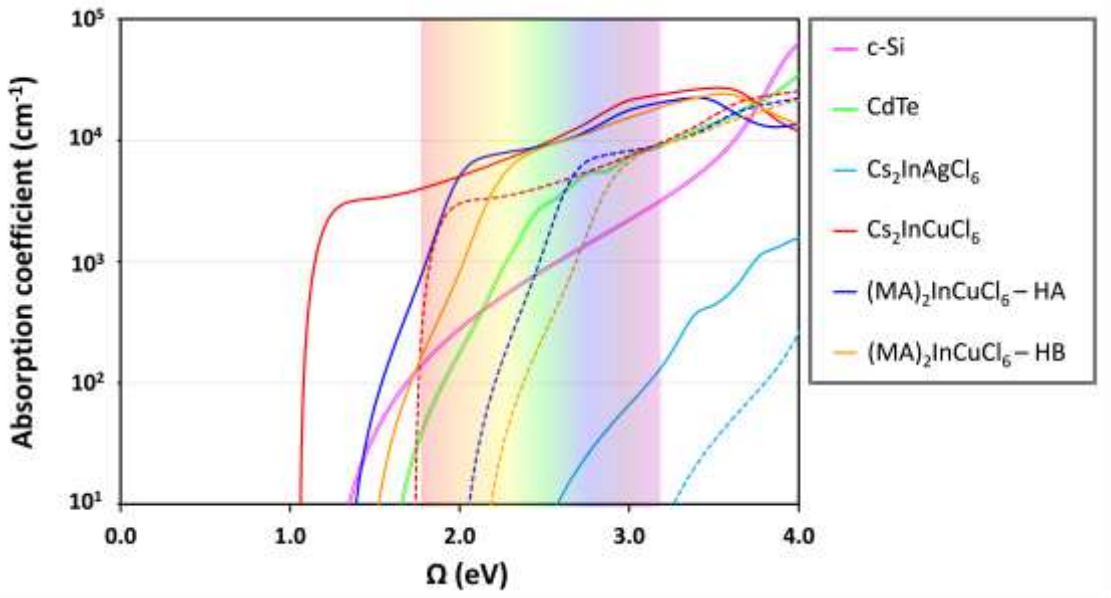

Fig. 7 Optical absorption coefficient for $Cs_2InCuCl_6$ and $(MA)_2InCuCl_6$. The absorption coefficients were computed at PBE level and shifted using a simple scissor correction with HSE06-SOC (solid curves) or PBE0-SOC (dash curves) band gaps.

The knowledge of band edge positions is important for designing solar cells and junctions in solar cells. Herein, we combine two different techniques to compute the absolute band edges: (i) surface band alignment[88, 89] for $Cs_2InCuCl_6$ and (ii) core-level alignment[90] for $(MA)_2InCuCl_6$ (HA and HB). Specifically, for $Cs_2InCuCl_6$ we construct and use a slab model to compute the absolute VBM and CBM energies with respect to the vacuum level. We use both HSE06 and PBE0 functional and neglect the effect of spin-orbit coupling due to the expensive cost of the slab calculation. This approach, however, is neither feasible nor straightforward for $(MA)_2InCuCl_6$ because of two issues. First, more than one slab model of $(MA)_2InCuCl_6$ need to be considered because the crystal structure with $CH_3NH_3^+$ ions is anisotropic. Second, the slab calculation using the hybrid functions (HSE06 or PBE0) for $(MA)_2InCuCl_6$ is even more costly than that for the inorganic derivative. Instead, we use the Cu *p* core level as the reference state for both $Cs_2InCuCl_6$ and $(MA)_2InCuCl_6$ and the absolute band edges of $(MA)_2InCuCl_6$ are determined using this electronic marker and the absolute band edges of $Cs_2InCuCl_6$. Details of the band edge calculations can be found in the **SI** Section S3.

Fig. 6 shows the band offsets for $Cs_2InCuCl_6$ and $(MA)_2InCuCl_6$ (HA and HB) computed in this work, and for other semiconductors, such as TiO_2 and $MAPbI_3$ from the literature for reference.[89] There is a negligible difference of ca. 0.1-0.2 eV between the band edges of $Cs_2InCuCl_6$ and $(MA)_2InCuCl_6$ regardless of the functional choice, reaffirming the unimportant role of the organic ions for determining electronic structure of the band edges in hybrid organic-inorganic perovskites. In general, the absolute energy of the VBM is within -4.3 and -4.1 eV and that of the CBM is between -6.2 and -6.1 eV. The CBM of $Cs_2InCuCl_6$ and $(MA)_2InCuCl_6$ are slightly lower than that of $MAPbI_3$ irrespective of whether HSE06 or PBE0 is used. In contrast, the VBM computed by PBE0 are significantly lower than the VBM of $MAPbI_3$ (about 0.7-0.8 eV) while HSE06 predicts a small difference of 0.2-0.3 eV. It is not feasible to comment on which functional is more accurate in this case due to the lack of experimental values.

3.4 Optical properties

We investigated the theoretical optical properties of $Cs_2InCuCl_6$ and $(MA)_2InCuCl_6$. We use the PBE functional to obtain the frequency-dependent dielectric matrix needed for the absorption coefficient calculation (see the **SI** Section S4) and the HSE06-SOC or PBE0-SOC band gaps (as discussed in the Computational method section) to plot the optical absorption coefficient shown in Fig. 7. The same calculations are conducted for the c-Si and CdTe and for the previously synthesized[34] double perovskite $Cs_2InAgCl_6$ to compare with $Cs_2InCuCl_6$ and $(MA)_2InCuCl_6$. Amongst all the materials in Fig. 7, $Cs_2InCuCl_6$ has the highest absorption coefficient irrespective of the functional choice for the band gap correction. Surprisingly, the $(MA)_2InCuCl_6$ absorption coefficient is higher than that of c-Si and CdTe despite the fact that $(MA)_2InCuCl_6$ is an indirect band gap material.

3.5 Intrinsic charge carrier mobility for $Cs_2InCuCl_6$

Finally, we discuss charge transport properties of $Cs_2InCuCl_6$.

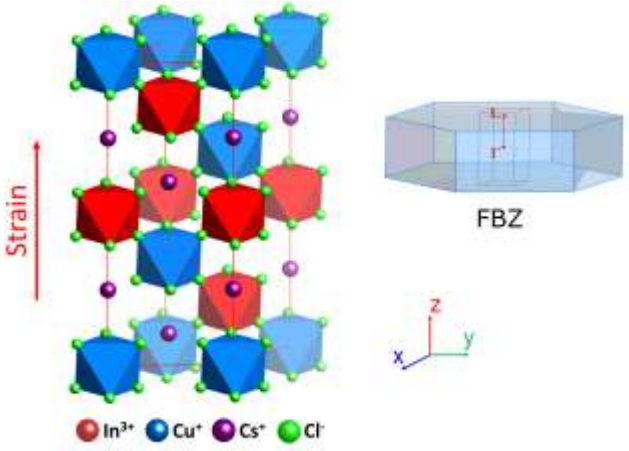

Fig. 8 Trigonal unit cell of $Cs_2InCuCl_6$ and its FBZ were used in calculating the charge mobility. A dilation $\Delta l/l_o$ (or strain) is applied along the z axis.

For the hybrid perovskite $(MA)_2InCuCl_6$, it is challenging to perform the same calculation due to the high computational cost. We only compute the mobility along the L-Γ path since the effective mass approximation cannot be applied for the flat valence band along the Γ-X path. The L-Γ path corresponds to a path along In, Cs, and Cu in the real space. To compute the intrinsic charge carrier mobility, we used the Boltzmann Transport Equation (BTE)[67] and the Deformation Potential (DP)[68] theory as discussed in the Computational Methods Section. The DP theory was originally devised to compute the mobility in non-polar crystals but has since been used to study charge transport in many other materials, including organic semiconductors,[91] graphene and graphene nanoribbons,[92] molybdenum disulfide,[93] and black phosphorus.[94] Recently, Zhao *et al.*[95] employed a similar approach to study intrinsic and extrinsic charge transport in $MAPbI_3$. Although this method has been successful in predicting intrinsic mobilities for low-dimensional materials, it can potentially carry large errors because carriers are assumed to scatter only from acoustic phonons. Other scattering mechanisms from optical phonons, defects, and impurities are neglected. Consequently, the experimentally measured mobilities turn out to be much smaller than the computed values. In practice the experimental mobilities vary with synthesis attesting to the importance of defects such as grain boundaries and impurities.[96] Considering these limitations, we chose to compare our calculated mobilities with the theoretical intrinsic mobility of $MAPbI_3$ reported in the literature.[95]

Table 3 Deformation potential constant (E_1), elastic constant (C), relaxation time (τ), and intrinsic mobilities (μ) for $Cs_2InCuCl_6$ at 300 K. The $MAPbI_3$ data is taken from the ref 93. A range for each quantity is given because charge transport is anisotropic in MAPbI3 crystal and values correspond to upper and lower bounds, or the fastest and slowest transport directions.

Material	Carrier	E_1 (eV)	C (GPa)	τ (ps)	μ ($cm^2/V\,s$)
$Cs_2InCuCl_6$	Electrons	4.09	62.0	0.776	4519
	Holes	1.94	62.0	0.649	1240
$MAPbI_3$	Electrons	0.4 – 4.9	7.5 – 22.5	0.12 – 0.33	572 – 2554
	Holes	0.6 – 2.2	7.5 – 22.5	0.67 – 1.87	1432 – 7176

Fig. 8 shows the trigonal $Cs_2InCuCl_6$ unit cell and its FBZ used in the transport calculation. In this unit cell, In, Cs, and Cu atoms are aligned (*i.e.,* the L-Γ path) along the z-axis. Thus, a dilation $\Delta l/l_o$, a strain, can be applied by simply varying the lattice parameter, c, and then calculating the deformation potential and the elastic constant in the manner described in the Computational Methods Section. Further details are also reported in Section S5 of the **SI**. Table 3 shows the deformation potential constant (E_1), the elastic constant (C), the relaxation time (τ), and the intrinsic mobility (μ) of holes and electrons for $Cs_2InCuCl_6$ at 300 K. We find that the electron and hole mobilities in $Cs_2InCuCl_6$ are approximately 4500 $cm^2.V^{-1}.s^{-1}$, and 1200 $cm^2.V^{-1}.s^{-1}$, respectively. These values are comparable to those calculated for $MAPbI_3$ for which the hole and electron mobilities are 1400-7000 $cm^2V^{-1}s^{-1}$ and 500-2500 $cm^2V^{-1}s^{-1}$,[95] respectively (the mobility values from the literature depends on transport direction, hence we provide them as a range to facilitate the comparison with our values). Regarding the deformation potential constant, both materials show strong scattering of electrons by lattice vibrations, *i.e.* large E_1 for electrons, presumably implying a lower electron mobility compared to that of the hole for $MAPbI_3$ and $Cs_2InCuCl_6$. Indeed, $MAPbI_3$ has lower electron mobilities than the hole mobilities. This trend, however, is reversed for $Cs_2InCuCl_6$ where electron mobilities are higher. The high electron mobilities in $Cs_2InCuCl_6$ can be explained by inspecting the effective mass. In fact, the hole effective mass (0.92 m_e) for $Cs_2InCuCl_6$ is three times larger than the electron effective mass (0.30 m_e), hence this large hole effective mass lowers the hole mobility. In contrast, the hole effective mass (0.25-0.60 m_e) for $MAPbI_3$ is only two times larger than the electron effective mass (0.15-0.30 m_e). (See Supplementary Information of ref [95]). To summarize, $Cs_2InCuCl_6$ exhibits charge mobilities comparable to $MAPbI_3$, which bodes well for its potential as a solar cell material. While we calculated charge transport along the L-Γ path we note that the hole mobility in $Cs_2InCuCl_6$ in other directions (*e.g.,* Γ-X path) may be smaller because the valence band is flatter along other directions, reducing the average hole mobility. Examining the curvature of the conduction band at the Γ point, we expect the electron mobility along Γ-X path to be similar to that along Γ-L path.

4. Conclusions

In summary, we have identified $Cs_2InCuCl_6$ as a promising semiconductor with a suitable band gap for solar cells. Its dynamic stability is confirmed by phonon calculations. We have shown that $Cs_2InCuCl_6$ and its hybrid derivative $(MA)_2InCuCl_6$ exhibit optimal band gaps and remarkable optical properties in comparison with other conventional semiconductors. Furthermore, charge transport in $Cs_2InCuCl_6$ is facile and this material is predicted to have an intrinsic charge carrier mobility similar to that of $MAPbI_3$ along the L-Γ path of the FBZ. Additionally, we have performed a band edge energy calculation for $Cs_2InCuCl_6$ and $(MA)_2InCuCl_6$ in order to inform future integration of these materials into solar cells. We anticipate the promising applications of these hypothetical compounds, if synthesized in the laboratory, as non-toxic semiconductors for developing optoelectronic devices.

Conflicts of interest

The authors declare no competing financial interest. The authors declare no competing financial interest.

Acknowledgements

This work was supported primarily by the National Science Foundation through the University of Minnesota MRSEC under Award Number DMR-1420013 and the iSuperseed program.

REFERENCES

1. W. Zhang, G. E. Eperon and H. J. Snaith, *Nat. Energy.*, 2016, **1**, 16048.
2. J. S. Manser, J. A. Christians and P. V. Kamat, *Chem. Rev.*, 2016, **116**, 12956.
3. P. D. Matthews, D. J. Lewis and P. O'Brien, *J. Mater. Chem. A*, 2017, **5**, 17135.
4. A. Kojima, K. Teshima, Y. Shirai and T. Miyasaka, *J. Am. Chem. Soc.*, 2009, **131**, 6050.
5. W. S. Yang, J. H. Noh, N. J. Jeon, Y. C. Kim, S. Ryu, J. Seo and S. I. Seok, *Science*, 2015, **348**, 1234.
6. M. A. Green, Y. Hishikawa, E. D. Dunlop, D. H. Levi, J. Hohl-Ebinger and A. W. Y. Ho-Baillie, *Prog Photovolt Res Appl.*, 2018, **26**, 427.
7. H. Tan, A. Jain, O. Voznyy, X. Lan, F. P. García de Arquer, J. Z. Fan, R. Quintero-Bermudez, M. Yuan, B. Zhang, Y. Zhao, F. Fan, P. Li, L. N. Quan, Y. Zhao, Z.-H. Lu, Z. Yang, S. Hoogland and E. H. Sargent, *Science*, 2017, **355**, 722.
8. NREL, *Journal*, 2018.
9. N. J. Jeon, J. H. Noh, W. S. Yang, Y. C. Kim, S. Ryu, J. Seo and S. I. Seok, *Nature*, 2015, **517**, 476.
10. G. E. Eperon, T. Leijtens, K. A. Bush, R. Prasanna, T. Green, J. T.-W. Wang, D. P. McMeekin, G. Volonakis, R. L. Milot, R. May, A. Palmstrom, D. J. Slotcavage, R. A. Belisle, J. B. Patel, E. S. Parrott, R. J. Sutton, W. Ma, F. Moghadam, B. Conings, A. Babayigit, H.-G. Boyen, S. Bent, F. Giustino, L. M. Herz, M. B. Johnston, M. D. McGehee and H. J. Snaith, *Science*, 2016, **354**, 861.
11. T. Leijtens, K. A. Bush, R. Prasanna and M. D. McGehee, *Nat. Energy.*, 2018, DOI: 10.1038/s41560-018-0190-4, 828.
12. T. C.-J. Yang, P. Fiala, Q. Jeangros and C. Ballif, *Joule*, 2018, **2**, 1421.
13. S. Patwardhan, D. H. Cao, S. Hatch, O. K. Farha, J. T. Hupp, M. G. Kanatzidis and G. C. Schatz, *J. Phys. Chem. Lett.*, 2015, **6**, 251.
14. A. Daus, C. Roldán-Carmona, K. Domanski, S. Knobelspies, G. Cantarella, C. Vogt, M. Grätzel, M. K. Nazeeruddin and G. Tröster, *Adv. Mater.*, 2018, **30**, 1707412.
15. Y.-H. Lin, P. Pattanasattayavong and T. D. Anthopoulos, *Adv. Mater.*, 2017, **29**, 1702838.
16. K. Lin, J. Xing, L. N. Quan, F. P. G. de Arquer, X. Gong, J. Lu, L. Xie, W. Zhao, D. Zhang, C. Yan, W. Li, X. Liu, Y. Lu, J. Kirman, E. H. Sargent, Q. Xiong and Z. Wei, *Nature*, 2018, **562**, 245.
17. Z.-K. Tan, R. S. Moghaddam, M. L. Lai, P. Docampo, R. Higler, F. Deschler, M. Price, A. Sadhanala, L. M. Pazos, D. Credgington, F. Hanusch, T. Bein, H. J. Snaith and R. H. Friend, *Nat. Nanotechnol.*, 2014, **9**, 687.
18. L. Zhang, X. Yang, Q. Jiang, P. Wang, Z. Yin, X. Zhang, H. Tan, Y. Yang, M. Wei, B. R. Sutherland, E. H. Sargent and J. You, *Nat. Commun.*, 2017, **8**, 15640.
19. Y. Jia, R. A. Kerner, A. J. Grede, B. P. Rand and N. C. Giebink, *Nat. Photonics*, 2017, **11**, 784.
20. B. R. Sutherland and E. H. Sargent, *Nat. Photonics*, 2016, **10**, 295.
21. G. Niu, X. Guo and L. Wang, *J. Mater. Chem. A*, 2015, **3**, 8970.
22. T. Leijtens, G. E. Eperon, N. K. Noel, S. N. Habisreutinger, A. Petrozza and H. J. Snaith, *Adv. Energy Mater.*, 2015, **5**, 1500963.
23. A. Babayigit, A. Ethirajan, M. Muller and B. Conings, *Nat. Mater.*, 2016, **15**, 247.
24. A. Babayigit, D. Duy Thanh, A. Ethirajan, J. Manca, M. Muller, H. G. Boyen and B. Conings, *Sci. Rep.*, 2016, **6**, 18721.
25. Y. Rong, Y. Hu, A. Mei, H. Tan, M. I. Saidaminov, S. I. Seok, M. D. McGehee, E. H. Sargent and H. Han, *Science*, 2018, **361**, 1.
26. D. Ray, C. Clark, H. Q. Pham, J. Borycz, R. J. Holmes, E. S. Aydil and L. Gagliardi, *J. Phys. Chem. C*, 2018, **122**, 7838.
27. M. R. Filip and F. Giustino, *J. Phys. Chem. C*, 2015, **120**, 166.
28. M. T. Klug, A. Osherov, A. A. Haghighirad, S. D. Stranks, P. R. Brown, S. Bai, J. T. W. Wang, X. Dang, V. Bulović, H. J. Snaith and A. M. Belcher, *Energy Environ. Sci.*, 2017, **10**, 236.
29. S. Chatterjee and A. J. Pal, *J. Mater. Chem. A*, 2018, **6**, 3793.
30. F. Giustino and H. J. Snaith, *ACS Energy Lett.*, 2016, **1**, 1233.
31. P. P. Boix, S. Agarwala, T. M. Koh, N. Mathews and S. G. Mhaisalkar, *J. Phys. Chem. Lett.*, 2015, **6**, 898.
32. J. Gebhardt and A. M. Rappe, *ACS Energy Lett.*, 2017, **2**, 2681.
33. H.-Y. Ye, Y.-Y. Tang, P.-F. Li, W.-Q. Liao, J.-X. Gao, X.-N. Hua, H. Cai, P.-P. Shi, Y.-M. You and R.-G. Xiong, *Science*, 2018, **361**, 151.
34. G. Volonakis, A. A. Haghighirad, R. L. Milot, W. H. Sio, M. R. Filip, B. Wenger, M. B. Johnston, L. M. Herz, H. J. Snaith and F. Giustino, *J. Phys. Chem. Lett.*, 2017, **8**, 772.
35. F. Locardi, M. Cirignano, D. Baranov, Z. Dang, M. Prato, F. Drago, M. Ferretti, V. Pinchetti, M. Fanciulli, S. Brovelli, L. De Trizio and L. Manna, *J. Am. Chem. Soc.*, 2018, **140**, 12989.
36. J. Dai, L. Ma, M. Ju, J. Huang and X. C. Zeng, *Phys. Chem. Chem. Phys.*, 2017, **19**, 21691.
37. G. Volonakis, M. R. Filip, A. A. Haghighirad, N. Sakai, B. Wenger, H. J. Snaith and F. Giustino, *J. Phys. Chem. Lett.*, 2016, **7**, 1254.
38. M. R. Filip, S. Hillman, A. A. Haghighirad, H. J. Snaith and F. Giustino, *J. Phys. Chem. Lett.*, 2016, **7**, 2579.
39. E. T. McClure, M. R. Ball, W. Windl and P. M. Woodward, *Chem. Mater.*, 2016, **28**, 1348.
40. A. H. Slavney, T. Hu, A. M. Lindenberg and H. I. Karunadasa, *J. Am. Chem. Soc.*, 2016, **138**, 2138.
41. C. N. Savory, A. Walsh and D. O. Scanlon, *ACS Energy Lett.*, 2016, **1**, 949.
42. T. Kirchartz and U. Rau, *Adv. Energy Mater.*, 2018, **8**, 1703385.
43. S. Rühle, *Solar Energy*, 2016, **130**, 139.
44. W. Shockley and H. J. Queisser, *J. Appl. Phys.*, 1961, **32**, 510.
45. M. Levy, *Proc. Natl. Acad. Sci. U.S.A.*, 1979, **76**, 6062.
46. P. Hohenberg and W. Kohn, *Phys. Rev.*, 1964, **136**, B864.
47. W. Kohn and L. J. Sham, *Phys. Rev.*, 1965, **140**, A1133.
48. Z. Xiao, K. Z. Du, W. Meng, J. Wang, D. B. Mitzi and Y. Yan, *J. Am. Chem. Soc.*, 2017, **139**, 6054.
49. X. G. Zhao, D. Yang, Y. Sun, T. Li, L. Zhang, L. Yu and A. Zunger, *J. Am. Chem. Soc.*, 2017, **139**, 6718.
50. T. Nakajima and K. Sawada, *J. Phys. Chem. Lett.*, 2017, **8**, 4826.
51. G. Kresse and J. Furthmüller, *Comput. Mater. Sci.*, 1996, **6**, 15.

52. G. Kresse and J. Furthmüller, *Phys. Rev. B*, 1996, **54**, 11169.
53. G. Kresse and J. Hafner, *Phys. Rev. B*, 1993, **47**, 558.
54. G. Kresse and D. Joubert, *Phys. Rev. B*, 1999, **59**, 1758.
55. J. P. Perdew, A. Ruzsinszky, G. I. Csonka, O. A. Vydrov, G. E. Scuseria, L. A. Constantin, X. Zhou and K. Burke, *Phys. Rev. Lett.*, 2008, **100**, 136406.
56. A. V. Krukau, O. A. Vydrov, A. F. Izmaylov and G. E. Scuseriaa, *J. Chem. Phys.*, 2006, **125**, 224106.
57. C. Adamo and V. Barone, *J. Chem. Phys.*, 1999, **110**, 6158.
58. A. Togo and I. Tanaka, *Scr. Mater.*, 2015, **108**, 1.
59. J. P. Perdew, K. Burke and M. Ernzerhof, *Phys. Rev. Lett.*, 1996, **77**, 3865.
60. J. P. Perdew, K. Burke and M. Ernzerhof, *Phys. Rev. Lett.*, 1997, **78**, 1396.
61. P. Mori-Sánchez, A. J. Cohen and W. Yang, *Phys. Rev. Lett.*, 2008, **100**, 146401.
62. L. J. Sham and M. Schlüter, *Phys. Rev. Lett.*, 1983, **51**, 1888.
63. J. P. Perdew and M. Levy, *Phys. Rev. Lett.*, 1983, **51**, 1884.
64. R. Dovesi, A. Erba, R. Orlando, C. M. Zicovich-Wilson, B. Civalleri, L. Maschio, M. Rérat, S. Casassa, J. Baima, S. Salustro and B. Kirtman, *Wiley Interdiscip. Rev. Comput. Mol. Sci*, 2018, **8**, e1360.
65. J. Laun, D. Vilela Oliveira and T. Bredow, *J. Comput. Chem.*, 2018, **39**, 1285.
66. M. F. Peintinger, D. V. Oliveira and T. Bredow, *J. Comput. Chem.*, 2013, **34**, 451.
67. P. Allen, *Boltzmann Theory, and Resistivity of Metals*, Kluwer academic publishers, Norwell, Massachusetts, USA, 1st Ed. edn., 1996.
68. J. Bardeen and W. Shockley, *Phys. Rev.*, 1950, **80**, 72.
69. V. M. Goldschmidt, *Naturwissenschaften*, 1926, **14**, 477.
70. O. Madelung, *Semiconductors: Data Handbook*, Springer, New York, 2004.
71. G. Fonthal, L. Tirado-Mejía, J. I. Marín-Hurtado, H. Ariza-Calderón and J. G. Mendoza-Alvarez, *J. Phys. Chem. Solids*, 2000, **61**, 579.
72. U.-G. Jong, C.-J. Yu, Y.-H. Kye, Y.-S. Kim, C.-H. Kim and S.-G. Ri, *J. Mater. Chem. A*, 2018, **6**, 17994.
73. Z. Xiao, K.-Z. Du, W. Meng, D. B. Mitzi and Y. Yan, *Angew. Chem. Int. Ed.*, 2017, **56**.
74. D. Han, T. Zhang, M. Huang, D. Sun, M.-H. Du and S. Chen, *APL Materials*, 2018, **6**.
75. Y. H. Chang, C. H. Park and K. Matsuishi, *J. Korean Phys. Soc.*, 2004, **44**, 889.
76. A. Poglitsch and D. Weber, *J. Chem. Phys.*, 1987, **87**, 6373.
77. L. D. Whalley, J. M. Frost, Y.-K. Jung and A. Walsh, *J. Chem. Phys.*, 2017, **146**, 220901.
78. A. M. A. Leguy, J. M. Frost, A. P. McMahon, V. G. Sakai, W. Kockelmann, C. Law, X. Li, F. Foglia, A. Walsh, B. C. O'Regan, J. Nelson, J. T. Cabral and P. R. F. Barnes, *Nat. Commun.*, 2015, **6**, 7124.
79. C. Quarti, E. Mosconi and F. De Angelis, *Phys. Chem. Chem. Phys.*, 2015, **17**, 9394.
80. L. Zhou, A. J. Neukirch, D. J. Vogel, D. S. Kilin, L. Pedesseau, M. A. Carignano, A. D. Mohite, J. Even, C. Katan and S. Tretiak, *ACS Energy Lett.*, 2018, **3**, 787.
81. W. A. Saidi and J. J. Choi, *J. Chem. Phys.*, 2016, **145**, 144702.
82. A. Stroppa, C. Quarti, F. De Angelis and S. Picozzi, *J. Phys. Chem. Lett.*, 2015, **6**, 2223.
83. C. Quarti, E. Mosconi and F. De Angelis, *Chem. Mater.*, 2014, **26**, 6557.
84. Z. Fan, J. Xiao, K. Sun, L. Chen, Y. Hu, J. Ouyang, K. P. Ong, K. Zeng and J. Wang, *J. Phys. Chem. Lett.*, 2015, **6**, 1155.
85. M. R. Filip, C. Verdi and F. Giustino, *J. Phys. Chem. C*, 2015, **119**, 25209.
86. L. Z. Tan, F. Zheng and A. M. Rappe, *ACS Energy Lett.*, 2017, **2**, 937.
87. J.-H. Lee, N. C. Bristowe, J. H. Lee, S.-H. Lee, P. D. Bristowe, A. K. Cheetham and H. M. Jang, *Chem. Mater.*, 2016, **28**, 4259.
88. Y. Hinuma, Y. Kumagai, I. Tanaka and F. Oba, *Phys. Rev. B*, 2017, **95**, 075302.
89. J. Even, L. Pedesseau, J.-M. Jancu and C. Katan, *J. Phys. Chem. Lett.*, 2013, **4**, 2999.
90. K. T. Butler, J. M. Frost and A. Walsh, *Mater. Horizons*, 2015, **2**, 228.
91. J. Xi, M. Long, L. Tang, D. Wang and Z. Shuai, *Nanoscale*, 2012, **4**, 4348.
92. M. Long, L. Tang, D. Wang, Y. Li and Z. Shuai, *ACS Nano*, 2011, **5**, 2593.
93. Y. Cai, G. Zhang and Y. W. Zhang, *J. Am. Chem. Soc.*, 2014, **136**, 6269.
94. J. Qiao, X. Kong, Z. X. Hu, F. Yang and W. Ji, *Nat. Commun.*, 2014, **5**, 4475.
95. T. Zhao, W. Shi, J. Xi, D. Wang and Z. Shuai, *Sci. Rep.*, 2016, **6**, 19968.
96. M. J. Deen and F. Pascal, *J. Mater. Sci. Mater. Electron.*, 2006, **17**, 549.

Table of Content Graphic

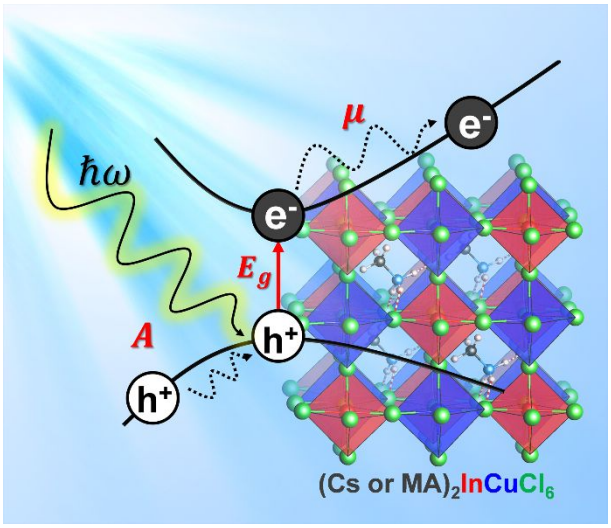

Two indium-based double perovskites, $Cs_2InCuCl_6$ and $(CH_3NH_3)_2InCuCl_6$, were proposed as promising materials for photovoltaic and optoelectronic applications with suitable band gap, exceptional optical and electrical properties.